Laser Physics, Vol. 6, No. 3, 1996, pp. 535–543.
Original Text Copyright © 1996 by Astro, Ltd.
Copyright © 1996 by МАИК Наука/Interperiodica Publishing (Russia).

COHERENT PHENOMENA AND HOLOGRAPHY

Photon Echo Modulation Effects in Cesium Vapor

A. I. Lvovsky and S. R. Hartmann

Physics Department, Columbia University, New York, NY, 10027 USA
e-mail: srh@phys.columbia.edu

Received January 29, 1996

Abstract—Photon echoes are generated on the $6S_{1/2}$–$6P_{1/2}$ transition in Cs vapor with excitation pulses short enough to excite all hyperfine states. As the excitation pulse separation is varied, the temporal profile of the echo reshapes and the time-integrated echo intensity modulates. These effects are typical of all the alkali vapors and provide the simplest, nontrivial display of quantum beating in a four-level system. The present paper describes a detailed experimental study of both kinds of modulation effects and utilizes the billiard ball model to analyze them.

INTRODUCTION

Photon echo experiments carried out on an optical transition whose terminal states are nondegenerate give rise to two kinds of modulation effects [1]. The first is the modulation of the time-integrated echo signal intensity as the excitation pulse separation is varied [2–4]; the second is the quantum beats displayed by the echo signal itself [4–6].

When many neighboring nuclei contribute to the hyperfine interactions, these effects are further enhanced and lead to the complicated modulation patterns observed in [3] and [6]. In an atomic vapor these enhancements are not present and the modulation behavior is amenable to exact calculation [4]. In this paper, we make a systematic experimental and theoretical study of quantum beat effects as they manifest themselves in photon echo experiments performed on simple four-level systems. We analyze these effects with the help of the billiard ball model (BBM) [7–9] and obtain excellent agreement between experiment and theory.

A SIMPLE SYSTEM: CESIUM VAPOR

We choose to work on the $6S_{1/2}$–$6P_{1/2}$ optical transition in Cs vapor, which is a simple four-level system. Cesium is the heaviest among alkalis, minimizing Doppler dephasing effects, and occurs as a single stable isotope. The hyperfine interaction splits the terminal levels and introduces both kinds of modulation effects.

Since the cesium nucleus has spin $I = 7/2$, the $6S_{1/2}$ and the $6P_{1/2}$ levels in the atom of neutral cesium are each split into two hyperfine sublevels with quantum numbers F equal to 3 and 4. For both $6S_{1/2}$ and $6P_{1/2}$, the sublevel with $F = 4$ has higher energy than the one with $F = 3$; the magnitude of splitting is 9.193 GHz for the ground state and 1.168 GHz for the excited state [10]. Each sublevel contains $(2F + 1)$ magnetic substates; we specialize to the case in which the excitation pulses are circularly polarized. If the quantization axis is chosen along the light propagation direction, the only nonvanishing transition matrix elements are those which couple the states $|L = 6S_{1/2}; F = 3, 4; m_F\rangle$ and $|L = P_{1/2}; F = 3, 4; m_F + 1\rangle$. It suffices to separately consider the echo formation process as it develops in clusters of just four levels (see Fig. 1).

THEORY (FULL ECHO ANALYSIS)

We begin by constructing billiard-ball (BB) recoil diagrams and associate a BB with each trajectory [7–9]. When BBs associated with different trajectories overlap, a macroscopic transition dipole moment develops whose amplitude is proportional to the overlap. If the macroscopic moment is phase-matched, coherent radiation ensues. For a simple two-level system, the ordinary two-pulse photon echo originates from a single crossing, which occurs at $t = 2\tau$ when resonant optical excitation pulses are applied at $t = 0$ and τ. For multilevel systems, such as we consider here, the situation is more complicated and it is possible for echoes to be generated at a variety of crossings, not necessarily at $t = 2\tau$.

Our analysis is for an arbitrary optical transition whose terminal states are split into two or more hyperfine sublevels. The theory simplifies for a 1/2–1/2 transition, which we illustrate for the $6S_{1/2}$–$6P_{1/2}$ transition in Cs vapor.

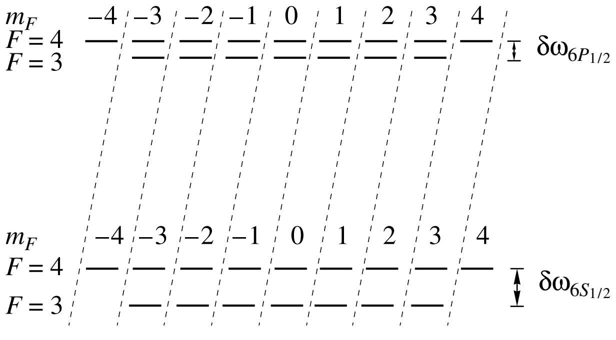

Fig. 1. Energy level diagram for Cs showing the individual hyperfine sublevels associated with the ground $6S_{1/2}$ and excited $6P_{1/2}$ states. For an atom initially in a particular hyperfine state, circularly polarized excitation pulses only generate superposition states within the same cluster (enclosed by the dashed lines).

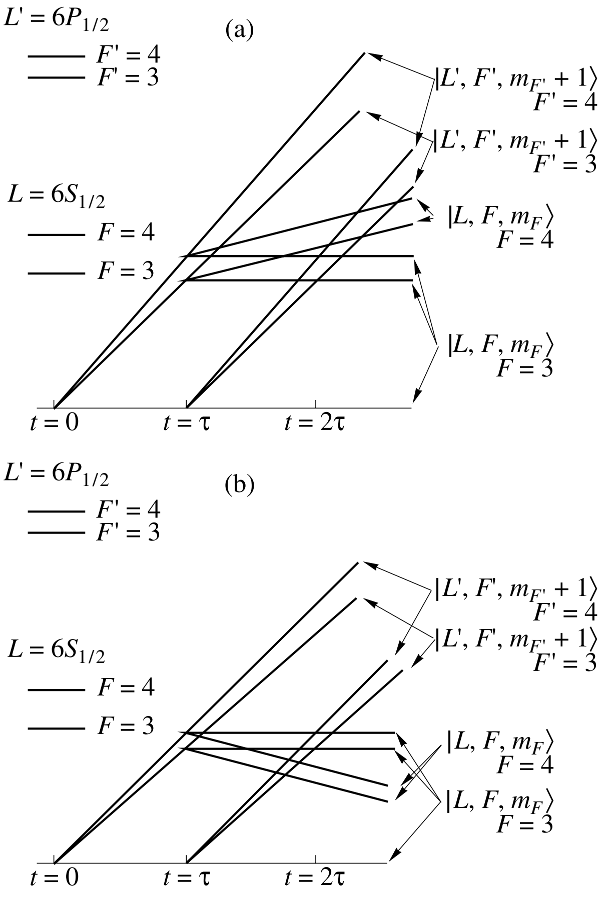

Fig. 2. Billiard ball diagrams associated with an optical $J = 1/2 \longrightarrow J = 1/2$ transition. Two classes of diagrams obtain according to whether the initial state, $|L, F, m_F\rangle$, corresponds to the lower [as in (a)] or upper [as in (b)] hyperfine sublevel.

We assume that the splitting of the ground state is small compared with k_BT, where k_B is the Boltzmann constant and T is the temperature at which the experiment is conducted. Since echo experiments are commonly preformed on samples in thermal equilibrium with their environment, all ground hyperfine states are uniformly populated. Therefore, the echo amplitude is the sum of equally weighted contributions from all initial states, in an arbitrary basis. In this section we choose the basis consisting of hyperfine states $|L, F, m_F\rangle$. In general, there are $(2F + 1)$ nondegenerate ground hyperfine states in each cluster, so that there are $(2F + 1)$ distinct recoil diagrams. We specialize, for the moment, to the recoil diagrams (Figs. 2a and 2b) that obtain for the $6S_{1/2}$–$6P_{1/2}$ transition in Cs vapor as they are only two in number and display the essential features of the more general case.

For simplicity, we assume that the excitation pulses are weak so that we have to present only those trajectories which are excited to the first order. We label each trajectory with the state to which it is associated. Referring again to Figs. 2a and 2b, we note that each diagram describes a situation in which the initial state $|6S_{1/2}, F, m_F\rangle$ is promoted by a series of two excitation pulses into a linear combination of $|6S_{1/2}, F, m_F\rangle$ and $|6P_{1/2}, F', m_F + 1\rangle$ with all possible values of F and F'. In all recoil diagrams, there are eight crossings in the neighborhood of $t = 2\tau$ (two crossings occur at exactly $t = 2\tau$) so that each diagram gives rise to eight contributions to the photon echo amplitude. Since the final ground and excited states have components with both $F = 3$ and 4, it follows that echo modulation components appear at both ground and excited state hyperfine splitting frequencies.

Associated with each trajectory there is a billiard ball whose density is given by $\rho(\mathbf{r} - \mathbf{r}_j) = (\sqrt{2/\pi}/R_{\mathrm{BB}})^{3/2} \times \exp[-(\mathbf{r} - \mathbf{r}_j)^2/R_{\mathrm{BB}}^2]$, where $R_{\mathrm{BB}} = \hbar/\sqrt{m_{\mathrm{Cs}} k_B T}$, m_{Cs} is the mass of the Cs atom, and j is the index of the trajectory. At $T = 300°$ K, $R_{\mathrm{BB}} = 3.5 \times 10^{-10}$ cm. When BBs of differing trajectories j and j' overlap, a macroscopic dipole moment is formed whose amplitude is proportional to the overlap, $f_{jj'} = \int \rho(\mathbf{r} - \mathbf{r}_j)\, \rho(\mathbf{r} - \mathbf{r}_{j'}) d^3\mathbf{r} = \exp[-(\mathbf{r}_j - \mathbf{r}_{j'})^2/2R_{\mathrm{BB}}^2]$, of the associated BBs [7–9]. In Figs. 3a and 3b, we draw the recoil diagram of Fig. 2a to scale and specialize to $\tau = 2$ ns. We have centered a BB

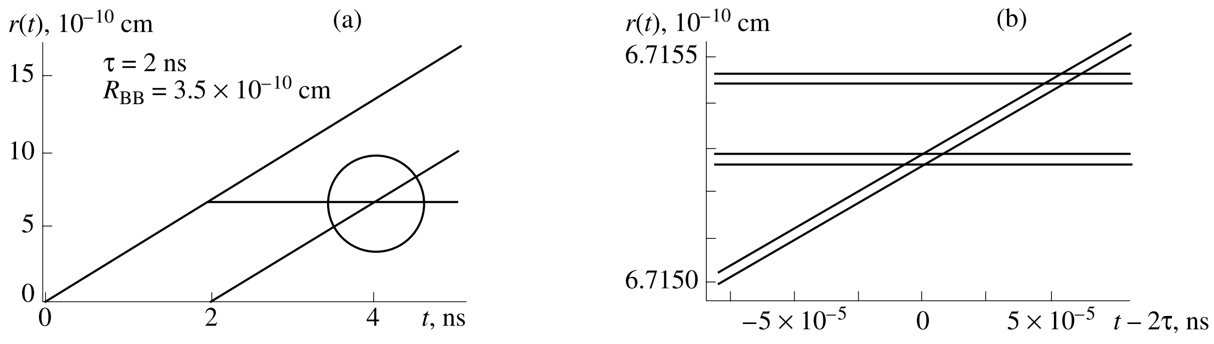

Fig. 3. A correctly scaled billiard ball diagram specialized to the Cs $6S_{1/2}$–$6P_{1/2}$ transition in a saturated vapor at 300° K for $\tau = 2$ ns. In (a) the BB diagram is displayed over the complete range. The structure displayed in Figs. 2a and 2b is unresolved. In (b) we specialize to the conditions of Fig. 2a and expand the scale to reveal the trajectory structure.

with radius R_{BB} at the crossing and in Fig. 3b have expanded the crossing region by a factor of $\cong 10^5$. In Fig. 3a, all detail relating to the separate hyperfine trajectories is unresolved. We note that R_{BB} is very large compared to the spread in times at which the separate crossings take place. We can therefore ignore any differences in the crossing times and in terms of billiard ball overlaps treat our diagram as a simple two-level photon echo diagram. The same comments apply to the appearance of the recoil diagram of Fig. 2b.

There are two trajectories, with indices 1 and 2, that lead to the photon echo generation, and we display them as heavy lines in Fig. 4. One diagram now suffices for all cases, and it is no longer necessary to be restricted to the simple $6S_{1/2}$–$6P_{1/2}$ transition. Since each propagator displayed represents one or more pairs of hyperfine states, we proceed by labeling each trajectory by the wave function associated with it. Initially we begin in the generic state $|L, F, m_F\rangle$; for Cs L would stand for $6S_{1/2}$, L' for $6P_{1/2}$ and F, F' for either 3 or 4. Along trajectory 1, this state evolves with an undiminished amplitude (we assumed that the excitation pulses are weak) so that up until $t = \tau$, it is given by

$$|\Psi_1^{(t<\tau)}(t)\rangle = \exp[-i\omega_{L,F}t]|L, F, m_F\rangle, \tag{1}$$

where $\hbar\omega_{L,F}$ is the energy of the state corresponding to the quantum numbers L and F.

At $t = \tau$, a resonant circularly polarized optical excitation pulse of area $\Theta_{F,m_F,F'}^{L,L'}(\tau)$ excites a linear combination of excited states $|L', F', m_F + 1\rangle$, $F' = 3$ and 4, which then develop according to $\exp[-i\omega_{L',F'}(t-\tau)]$ to yield

$$\begin{aligned}|\Psi_1^{(t>\tau)}(t)\rangle &= \frac{i}{2}\exp[-i\omega_{L,F}\tau] \\ &\times \sum_{F'}\Theta_{F,m_F,F'}^{L,L'}(\tau)\exp[-i\omega_{L',F'}(t-\tau)]|L', F', m_F+1\rangle.\end{aligned} \tag{2}$$

The evolution along trajectory 2 is initiated by the first excitation pulse of area $\Theta_{F,m_F,F'}^{L,L'}(0)$ and leads to an excited-state evolution

$$\begin{aligned}|\Psi_2^{(t<\tau)}(t)\rangle &= \frac{i}{2}\sum_{F'}\Theta_{F,m_F,F'}^{L,L'}(0) \\ &\times \exp[-i\omega_{L',F'}t]|L', F', m_F+1\rangle,\end{aligned} \tag{3}$$

which at $t = \tau$ is deexcited into a ground state superposition that evolves according to

$$\begin{aligned}|\Psi_2^{(t>\tau)}(t)\rangle &= \frac{1}{4}\sum_{F'}\sum_{F''}\Theta_{F,m_F,F'}^{L,L'}(0)\Theta_{F',m_F+1,F''}^{L,L'}(\tau) \\ &\times \exp[-i\omega_{L',F'}\tau]\exp[-i\omega_{L,F''}(t-\tau)]|L, F'', m_F\rangle.\end{aligned} \tag{4}$$

The dipole moment that is formed after the second excitation pulse is proportional to $\exp[-(\mathbf{r}_1(t) - \mathbf{r}_2(t))^2/(2R_{\mathrm{BB}}^2)]\langle\Psi_1^{(t>\tau)}(t)|P|\Psi_2^{(t>\tau)}(t)\rangle$, where $\mathbf{r}_1(t) - \mathbf{r}_2(t)$ is the displacement of trajectories 1 and 2 at time t [7–9]. The matrix element is given by

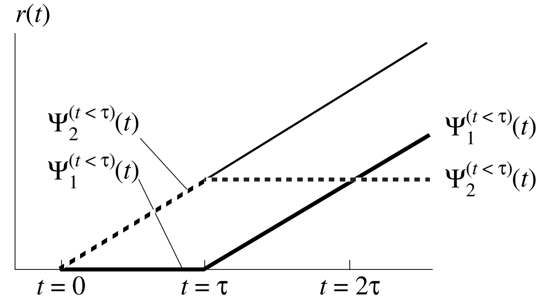

Fig. 4. The elementary billiard ball diagram shows the two trajectories that lead to photon echoes. The heavy solid line trajectory corresponds to Ψ_1, the dashed to Ψ_2.

$$\begin{aligned}\langle\Psi_1^{(t>\tau)}(t)|P|\Psi_2^{(t>\tau)}(t)\rangle &= -\frac{i}{8}\exp[i(\omega_L - \omega_{L'})(t-2\tau)] \\ &\times \sum_{F,m_F,F',F'',F'''}\{\langle L', F', m_F+1|P|L, F''', m_F\rangle \\ &\times \Theta_{F,m_F,F'}^{L,L'*}(\tau)\Theta_{F,m_F,F''}^{L,L'}(0)\Theta_{F'',m_F+1,F'''}^{L',L}(\tau) \\ &\times \exp[i\delta\omega_{L,F}\tau]\exp[i\delta\omega_{L',F'}(t-\tau)] \\ &\times \exp[-i\delta\omega_{L',F''}\tau]\exp[-i\delta\omega_{L,F'''}(t-\tau)]\},\end{aligned} \tag{5}$$

where $\omega_L = (\sum_F \omega_{L,F})/(2L+1)$; $\delta\omega_{L,F} = \omega_{L,F} - \omega_L$.

The photon echo intensity can be calculated from

$$\begin{aligned}I(t) &\approx \exp[-(\mathbf{r}_1(t) - \mathbf{r}_2(t))^2/R_{\mathrm{BB}}^2] \\ &\times \left|\langle\Psi_1^{(t>\tau)}(t)|P|\Psi_2^{(t<\tau)}(t)\rangle\right|^2\end{aligned} \tag{6}$$

and involves a sum over many states. This is the formula we use to compare with our measurements of the photon echo intensity in Cs vapor.

In calculating (6), it is useful to note that the excitation pulse area $\Theta_{F,m_F,F'}^{L,L'}$ is proportional to the transition matrix element:

$$\begin{aligned}&\langle L', F', m_F+1|P|L, F, m_F\rangle \\ &= \sum_{m_j}\langle L', F', m_F+1\,|\,L', m_j, I, m_I = m_F - m_j\rangle \\ &\times M_{m_j}\langle L, m_j+1, I, m_I = m_F - m_j\,|\,L, F, m_F\rangle,\end{aligned} \tag{7}$$

where $M_{m_j} = \langle L', m_j|P|L, m_j+1\rangle$ is independent of m_I and F and can be calculated from the Wigner–Eckart theorem. We use this relation to simplify (5) in the case of Cs.

Specializing to 1/2 ⟶ 1/2 Transition

We use (7) to obtain a simple expression for (5) when specializing to the $6S_{1/2}$–$6P_{1/2}$ cesium transition:

$$\langle\Psi_1^{(t>\tau)}|P|\Psi_2^{(t>\tau)}\rangle = -\frac{i}{8}\exp[i(\omega_{6P_{1/2}}-\omega_{6S_{1/2}})(t-2\tau)]$$
$$\times M_0|\Theta_2|^2\Theta_1\sum_{m_F}\tilde{G}_{6S_{1/2},-1/2}^{m_F-1/2*}(\tau)\tilde{G}_{6P_{1/2},+1/2}^{m_F-1/2*}(t-\tau) \quad (8)$$
$$\times\tilde{G}_{6P_{1/2},+1/2}^{m_F-1/2}(\tau)\tilde{G}_{6S_{1/2},-1/2}^{m_F-1/2}(t-\tau),$$

where we have defined

$$\tilde{G}_{L,\pm1/2}^{m_I}(t) = \sum_{F=3,4}\exp[-i\delta\omega_{L,F}t](C_{\pm1/2,m_I}^{F,m_I\pm1/2})^2, \quad (9)$$

where Θ_1 and Θ_2 are dimensionless quantities and $(C_{\pm1/2,m_I}^{F,m_I\pm1/2})$ is a Clebsch–Gordon coefficient. The physical reason underlying this simplicity will be discussed in the last chapter of the paper.

SIMPLE ECHO ANALYSIS

We can gain some insight into the echo behavior by studying the quantity

$$Q(t) \equiv -\frac{i}{8}\sum_{F,F',F'',F'''}\exp[i\delta\omega_{L,F}\tau]\exp[i\delta\omega_{L',F'}(t-\tau)]$$
$$\times\exp[-i\delta\omega_{L',F''}\tau]\exp[-i\delta\omega_{L,F'''}(t-\tau)], \quad (10)$$

which is how the rephased dipole moment (5) for one cluster would reform if all matrix elements were equal to unity.

$6S_{1/2}$–$6P_{1/2}$ Cs Transition

On specializing to the $6S_{1/2}$–$6P_{1/2}$ transition, (10) becomes

$$Q(t) = -\frac{i}{8}2^4\cos\frac{\delta\omega_L}{2}\tau\cos\frac{\delta\omega_L}{2}(t-\tau)$$
$$\times\cos\frac{\delta\omega_{L'}}{2}\tau\cos\frac{\delta\omega_{L'}}{2}(t-\tau). \quad (11)$$

Here, we have defined $\delta\omega_L = \omega_{L,4} - \omega_{L,3}$. The echo intensity would then follow

$$I(t) \approx \exp[-(\mathbf{r}_1(t)-\mathbf{r}_2(t))^2/R_{\mathrm{BB}}^2]Q^2(t)$$
$$= \frac{1}{4}f^2(t-2\tau)S(\tau)S(t-\tau), \quad (12)$$

where f is the overlap factor,

$$f^2(t-2\tau) = \exp[-(k_BTk^2/m_{\mathrm{Cs}})(t-2\tau)^2], \quad (13)$$

and S controls the beating,

$$S(t) \equiv (1-\cos\delta\omega_Lt)(1-\cos\delta\omega_{L'}t). \quad (14)$$

It is instructive to examine this expression because it gives insight into the manner in which the modulation effects are produced. In addition, although the expression is clearly a gross oversimplification, in the majority of cases, as we shall see, it gives quite accurate results.

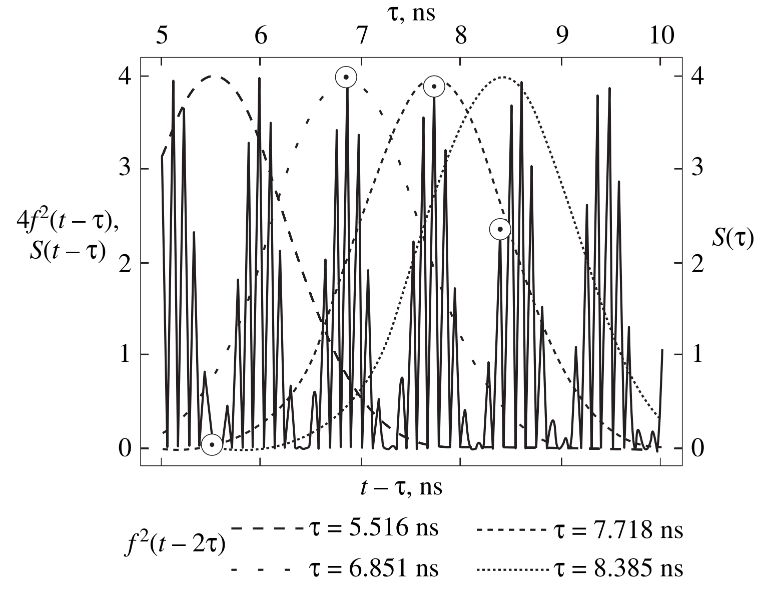

Fig. 5. Decomposition of equation (12). The functions $4f^2(t-2\tau)$ and $S(t-\tau)$ are plotted as a function of $t-\tau$, while $S(\tau)$ is plotted as a function of τ. The position of $4f^2(t-2\tau)$ depends on the choice of τ. We have chosen to display $4f^2(t-2\tau)$ for the τ 5.516, 6.851, 7.718, and 8.385 ns for which we have experimental results. The amplitude of $S(\tau)$, which determines the overall amplitude of the photon echo, has been marked by a circle at each of τ. It lies directly below the peak of the corresponding function $4f^2(t-2\tau)$. As τ increases, the function $4f^2(t-2\tau)$ moves to the right.

In Fig. 5, we plot $f^2(t-2\tau)$ and $S(t-\tau)$ as a function of $t-\tau$ and $S(\tau)$ as a function of τ. We vary the argument of S over the range of 5 to 10 ns. In displaying $f^2(t-2\tau)$, we choose the four cases $\tau = 5.516$, 6.851, 7.718, and 8.385 ns, which we are able to compare with experiment. For each of the four values of τ, we circle the corresponding point on the $S(\tau)$ plot. This value of $S(\tau)$ determines the overall magnitude of the echo intensity for the τ chosen. The temporal shape of the echo is determined by the product $f^2(t-2\tau)S(t-\tau)$. This product can be estimated by visual inspection of Fig. 5.

As we increase τ, the curve $f^2(t-2\tau)$, which peaks at $t-\tau=\tau$, moves to the right in Fig. 5. The modulation of the intensity follows $S(t-\tau)$, which has frequency components at both the ground and excited state hyperfine splitting frequencies. In order to follow the temporal display exactly, very fast detectors would be required. The detectors available to us in this experiment were able to resolve beats at the excited but not ground state splitting frequency. The information on high-frequency modulation is more readily available by measuring the integrated echo intensity as a function of τ. In this case, slow detectors suffice.

EXPERIMENTAL APPARATUS

A Spectra-Physics series 3000 actively mode-locked Nd:YAG laser was used to produce a train of 80 ps pulses separated by 12 ns. The pulse train was frequency doubled to 532 nm in a KDP crystal; the average output power was 1W. After attenuation by a factor of 2, the pulses were used to synchronously pump a Spectra-Physics 375B dye laser, which was tuned to the $\lambda = 894$ nm $6P_{1/2}$–$6S_{1/2}$ transition in cesium. This laser produced a train of 10-ps pulses which were close to transform-limited. These pulses were then spectrally filtered [11], amplified in a Quanta-Ray pulsed dye amplifier, spatially filtered, and divided along two beams of equal intensity (Fig. 6). One beam passed through a delay line composed of a mirror and a retroreflector. The mount of the retroreflector was movable along a rail, which was carefully aligned so that the direction and position of the delayed beam did not change with the magnitude of the delay. The two beams were then recombined with another beamsplitter and directed to a 1-cm quartz-walled cell containing saturated cesium vapor at room temperature. The angle between the beams was equal to $\phi = 5$ mrad, which satisfies the coherence condition [12], $\phi^2 \ll \lambda/L$, where $L = 1$ cm is the thickness of the cell. Photon echoes emerging from the cell were spatially filtered, in order to facilitate in blocking the excitation pulses, and focused on a EG&G C30971E photodiode (“fast FND”) with 1 GHz bandwidth. The pump intensity was also monitored with the EG&G FND-100 photodiode (“slow FND”).

EXPERIMENT

The experiment consisted of two parts: (1) In the first, we investigated temporal profiles of the echoes. The output of the “fast FND” photodetector was fed into the 1-GHz Tektronix 7A29 amplifier mounted in the 7104 oscilloscope mainframe. The waveforms appearing on the oscilloscope screen were recorded by a Tektronix digital camera system and stored in the computer’s memory for further analysis. For each position of the retroreflector, six waveforms were taken. (2) In the second part of the experiment we studied the dependence of the time-integrated echo intensity on the separation between the excitation pulses. The fast and slow FND outputs were directed into Stanford Research System gated integrators. The gate width was 40 ns for the pump and 7 ns for the echo detector. The output of the gated integrators was digitized and recorded. For each position of the retroreflector, 1000 measurements were made.

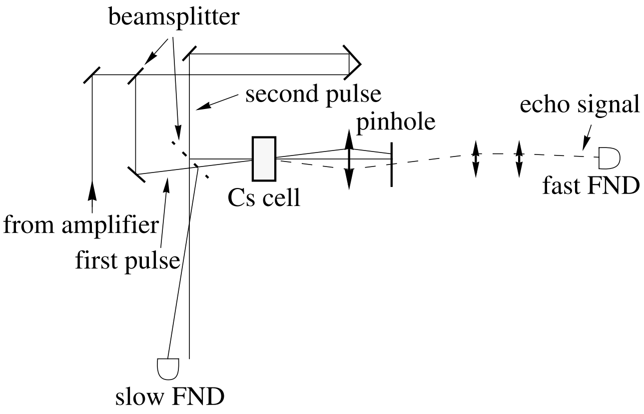

Fig. 6. A schematic diagram shows the essential elements of the photon echo experiment.

The delay between the excitation pulses was measured as follows. The retroreflector was set to a position that provided close but separated traces of the excitation

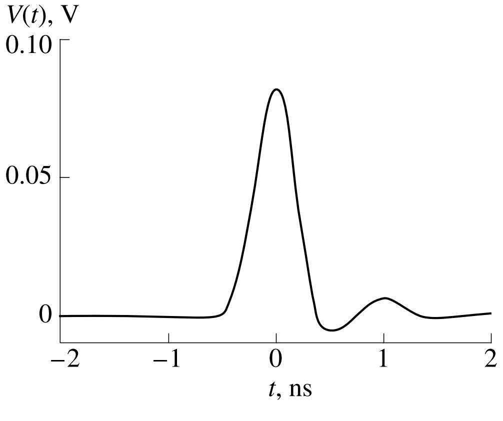

Fig. 7. The detector response function as displayed on a Tektronix 7104 mainframe using a 7A29 input amplifier. It responds to the output of a 1-GHz-bandwidth “fast FND” which is irradiated by a 10-ps optical excitation pulse. The zero of time is chosen at the peak of the response so that the displayed intensity will appear undelayed by the “slow” detector response. This facilitates a comparison between experimental measurements and theory.

pulses on the oscilloscope screen. The distance between the maxima of these traces provided the pulse separation at this reference point. Assuming perfect linearity for the oscilloscope time base, the ±2% (20 ps) Tektronix time base calibration uncertainty was the most significant source of error in this measurement. With this fixed point and precise measurement of the position of the retroreflector along the rail, the time delay between any pair of the excitation pulses could be determined to within the 20 ps uncertainty of the time base calibration.

Each oscilloscope trace can show (on an expanded scale) the photon echo preceded by the two excitation pulses which leak through the "blocking" aperture. The latter, being short, provide us with the detector response function $V(t)$ (see Fig. 7). This we convolve with the calculated response $I(t)$, equation (6), to produce the detector modified response

$$I_{\text{det}}(t) = \int I(t')V(t-t')dt', \tag{15}$$

which we can compare with experiment. Note that we have set the argument of $V(t)$ equal to zero at the peak of $V(t)$ so that both $I(t)$ and $I_{\text{det}}(t)$ are centered at $t = 2\tau$.

RESULTS (TEMPORAL PHOTON ECHO PROFILE)

Photon echo oscilloscope traces are shown in Figs. 8a–8d for excitation pulse separations of $\tau = 5.516$,

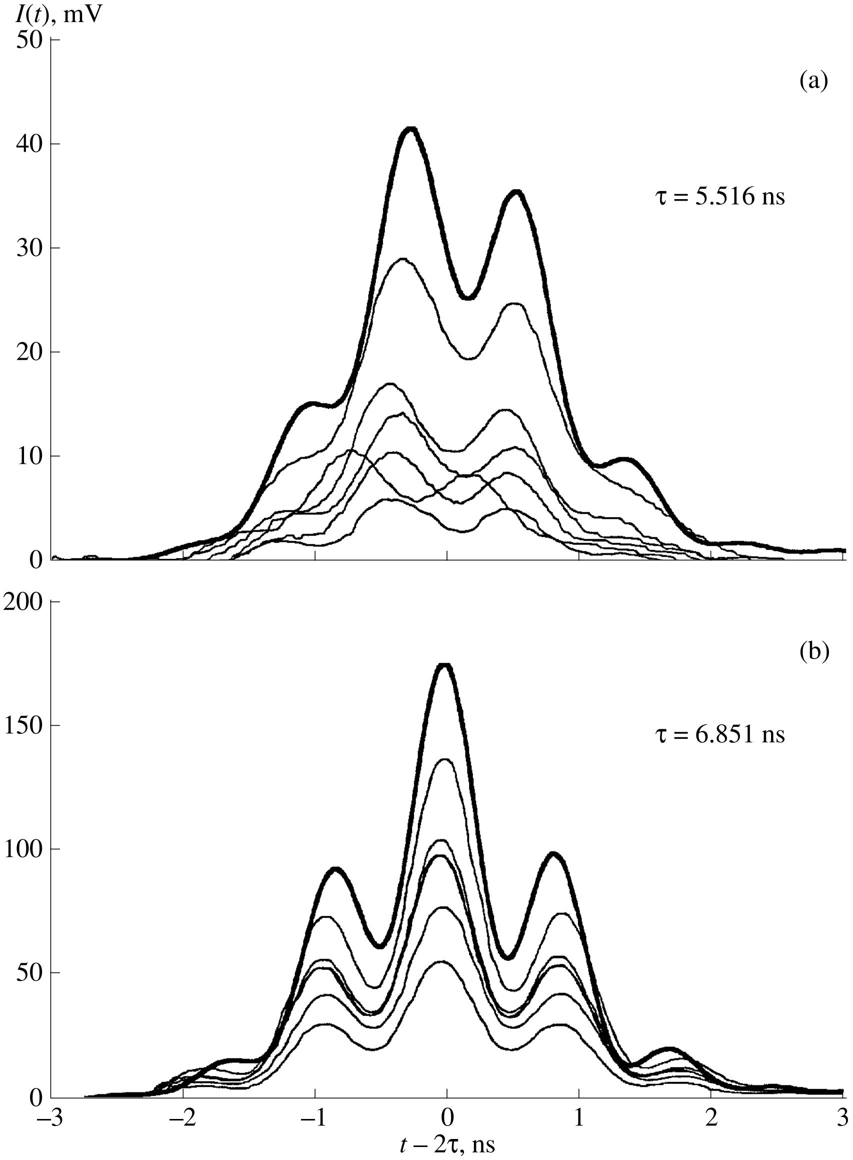

Fig. 8. Experimental photon echo traces plotted $t - 2\tau$ are presented for τ equal to 5.516, 6.851, 7.718, and 8.385 ns in (a–d). The heavy traces show $AI_{\text{det}}(t)$, where A is a normalization to facilitate comparison with experiment. The renormalization factor is the same in all four graphs.

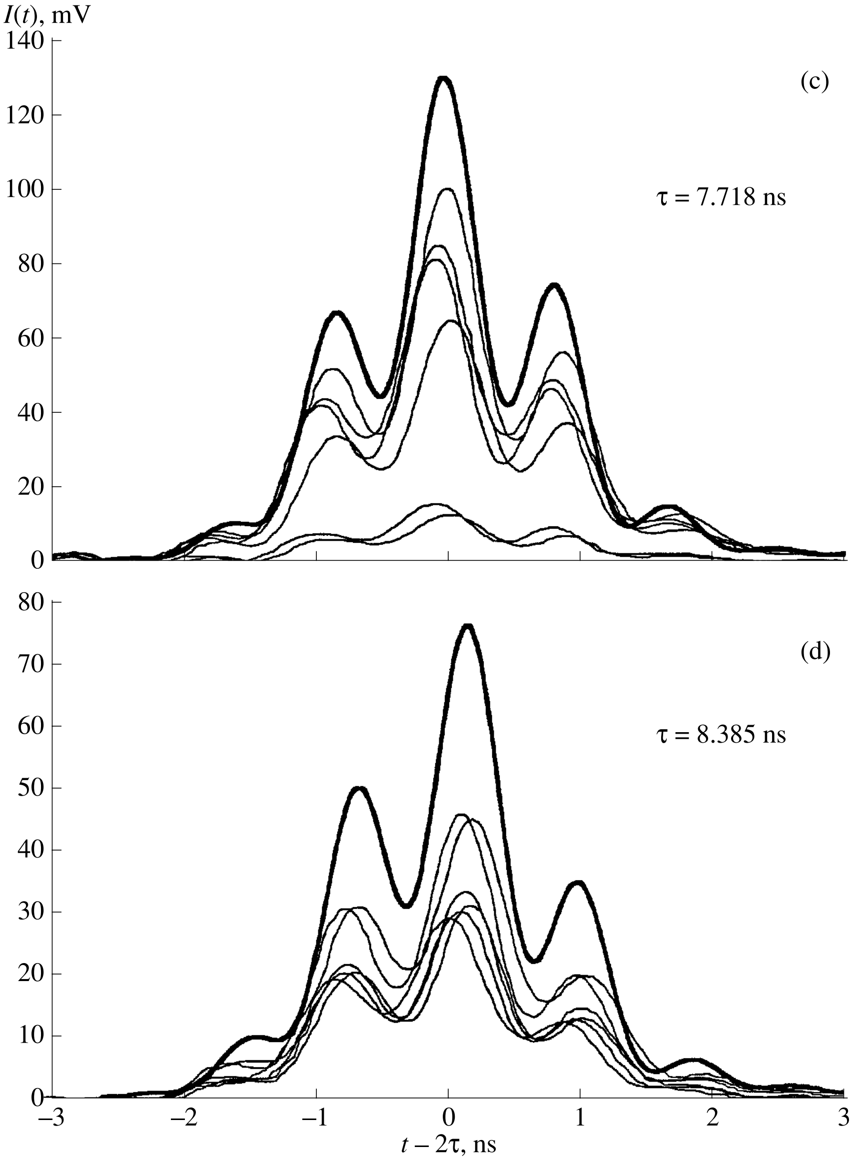

Fig. 8. (Contd.)

6.851, 7.718, and 8.385 ns. The traces show the temporal beating associated with the excited state hyperfine splitting. For each value of τ, we calculated the response $I_{\mathrm{det}}(t)$ of equation (15). We calculated the response over a spread of τ and found the best fit obtained when we made an 18 ps correction. The above list of τ incorporates this correction. The resulting calculated response was normalized and presented as the heavy line trace. It is clear that excellent agreement between experiment and theory is achieved.

Inherent in our analysis is the assumption that the sample is optically thin and excitation pulse areas are small enough to justify neglect of second-order effects. The intensity of the excitation pulses fluctuated considerably and led to a corresponding fluctuation in the photon echo amplitude. The independence of the temporal echo shape for the various traces we observed argues that the excitation pulse areas are small in the most of the excited volume. These separate traces are due in large part to variations in pump intensity which would lead to differing temporal pulse profiles if we were not in the small pulse area regime. To test for pulse propagation effects, we heated the sample and found no changes in temporal profile as long as the sample temperature was less than 315 K.

RESULTS (INTEGRATED PHOTON ECHO RESPONSE)

The integrated echo response as measured by the 7-ns gate and averaged over 1000 measurements is presented in Fig. 9. We swept τ from 6 to 8 ns readjusting the laser alignment at 7.3 ns to correct for slight drift in

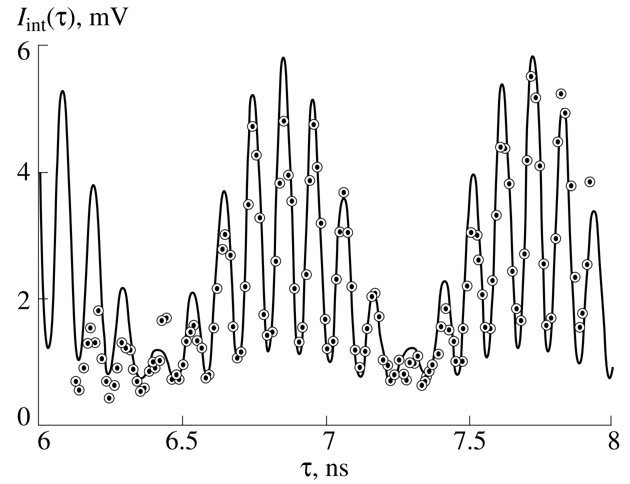

Fig. 9. Experimental data shows the integrated echo intensity as a function of τ. The solid trace is $A'I_{\text{int}}(\tau)$, where A' is a normalization constant.

the pump intensity. The temporally integrated (over the duration of the echo) echo response

$$I_{\text{int}}(\tau) = \int I_{\text{det}}(t)dt \tag{16}$$

was calculated, normalized, and shown as a solid line. The result of this calculation has been renormalized to facilitate comparison with the data. The experimental trace was shifted by somewhat less than 20 ps to improve the fit. As expected we now observe modulations at both the ground and excited state hyperfine splitting frequencies. Again, we obtain good agreement between experiment and calculation, except the region $6 < \tau < 6.4$ ns, where the pump laser did not function properly.

The data of Fig. 9 shows no indication of any overall decay, thus justifying our neglect of any homogeneous T_2 process.

DISCUSSION (FULL versus SIMPLE THEORY)

In addition to obtaining excellent agreement between experiment and the full theory (which respects the differences in the transition matrix elements involved in the photon echo process), we find that the simple theory [which leads to expression (11) and the results presented in Fig. 5] is surprisingly faithful to experiment. The major features of the experimental modulation pattern displayed in Fig. 9 are also found in Fig. 5. The main discrepancy is to be found in the region where the expected echo signals are small. For example, the magnitude of the calculated simple model response for $\tau = 5.516$ ns is much too low. This is not surprising, as the interferences, which reduce signal intensity, wash out when allowance is made for a variation in matrix element magnitudes. The measured temporal echo waveforms displayed in Fig. 8 agree very well with what would be predicted from the simple theoretical traces of Fig. 5. Once the effect of detector bandwidth is appreciated, it is clear that the major modulation features are accounted for.

THEORY (SPECIALIZED FOR THE Cs 1/2 ⟶ 1/2 TRANSITION)

In deriving equation (6), we used the "natural" basis consisting of the energy eigenstates $|L, F, m_F\rangle$ and exploited the fact that the BB radius, R_{BB}, was large compared to the region in which the separate trajectories crossed. The slightly diverging neighboring trajectories could then be considered degenerate and the recoil diagram in Fig. 4 reduced to that for a two-level system. Each trajectory then described a coherent superposition state associated with a particular m_F and all Fs. This simplification, notwithstanding, still leads to a formula, equation (6), which involves, even for the $6S_{1/2}$–$6P_{1/2}$ transition, multiple sums over hyperfine states. But since the trajectories are effectively degenerate, another way of dealing with this transition is instead to use the atomic states $|L, J, m_J, I, m_I\rangle$ since m_I does not change in an optical transition. There is then only one transition matrix element $\langle 6P_{1/2}, +1/2|P|6S_{1/2}, -1/2\rangle$. The analysis follows as before except that we now deal only with atomic states and we only keep those terms which ultimately contribute to the transition dipole moment. For a given m_I, there are initially two ground states: $|6S_{1/2}, -1/2\rangle$ and $|6S_{1/2}, +1/2\rangle$. Since circularly polarized excitation pulses have to increase m_J by 1, the second state does not participate in the echo formation process and can be dropped. Therefore, following the previous notation we write, in place of equation (1),

$$|\Psi_1^{(t<\tau)}(t)\rangle = G_{6S_{1/2}, -12}^{m_I}(t)|6S_{1/2}, -1/2, m_I\rangle, \tag{17}$$

where

$$\begin{aligned} G_{L, \pm 1/2}^{m_I}(t) &= \langle L, \pm 1/2, m_I|e^{-i\hat{H}t/\hbar}|L, \pm 1/2, m_I\rangle \\ &= \sum_{F=3,4} \exp[-i\omega_{L,F}t](C_{\pm 1/2, m_I}^{F, m_I \pm 1/2})^2 \\ &= \exp[-i\omega_L t]\tilde{G}_{L, \pm 1/2}^{m_I}(t) \end{aligned} \tag{18}$$

is the Green function for a recoil diagram propagator, and $\hat{H}$ is the Hamiltonian. In writing equation (17), we have omitted the term proportional to $|6S_{1/2}, +1/2, m_I - 1\rangle$ since we anticipate the action of the circularly polarized excitation pulse to be applied at $t = \tau$, which does not connect it to any excited state. Thus, there is no reason to carry it along. In contrast to the behavior of equation (1), the state associated with the first part of trajectory 1 in Fig. 4 is amplitude modulated according to equation (18). This is because $|6S_{1/2}, -1/2, m_I\rangle$ is not an eigenstate of the Hamiltonian. The Green function gives the factor by which its amplitude is diminished because of transfer to $|6S_{1/2}, +1/2, m_I - 1\rangle$. After the excitation pulse at $t = \tau$, we obtain the state

$$|\Psi_1^{(t>\tau)}(t)\rangle = \frac{i}{2}G^{m_I}_{6S_{1/2},-1/2}(\tau)\Theta_2 G^{m_I}_{6P_{1/2},+1/2}(t-\tau) \times |6P_{1/2}, 1/2, m_I\rangle. \tag{19}$$

Proceeding in a similar manner, we find for the final leg of trajectory 2:

$$|\Psi_2^{(t>\tau)}(t)\rangle = -\frac{1}{4}\Theta_1 G^{m_I}_{6P_{1/2},+1/2}(\tau)\Theta_2^* G^{m_I}_{6S_{1/2},-1/2}(t-\tau) \times |6P_{1/2}, -1/2, m_I\rangle. \tag{20}$$

In equations (19) and (20), Θ_1 and Θ_2 are the areas of the first and second excitation pulses with respect to the transition $|6S_{1/2}, -1/2, m_I\rangle \longrightarrow |6P_{1/2}, 1/2, m_I\rangle$. These quantities are the same for all values of m_I. Using (19) and (20), we obtain the transition dipole moment (8) directly.

DISCUSSION

The method presented here is somewhat different from that used in the conventional BBM. In the latter, one deals directly with stationary states for which there is a well-defined BB trajectory. The atomic states, on the other hand, are not eigenstates and have no precise recoil velocity or trajectory. However, the uncertainty in the trajectory for these states is much smaller than R_{BB} (Fig. 3) and therefore is negligible. We express this as

$$\delta V_{\text{recoil}}\tau = \frac{\hbar\delta\omega_L}{cm_{\text{Cs}}} \ll R_{\text{BB}}. \tag{21}$$

We also require that all the excitation pulses are short enough to excite all hyperfine states.

A significant advantage of the method presented here is that the photon echo process is directly interpretable as a modulation in the state amplitudes (19) and (20). This is not intuitively displayed in the eigenstate amplitudes (2) and (4). In the latter case it is necessary to take linear combinations of state amplitudes to obtain the same visualization.

It is to be noted that the method can be easily generalized to situations where there are more than two hyperfine sublevels associated with each energy level. However, the complexity of the resulting expressions increases rapidly with the number of sublevels.

ACKNOWLEDGMENTS

We appreciate experimental assistance from Dr. J.H. Brownell and stimulating discussions with Professor R. Friedberg. A.L. thanks Professor B. Brody for helpful discussions. This work was supported by the Army Research Office and the National Science Foundation, grant no. PHY-91-22388.

REFERENCES

1. Alekseyev, A.I., 1970, *Phys. Lett. A*, **31**, 495.
2. Meth, S. and Hartmann, S.R., 1978, *Opt. Commun.*, **24**, 100.
3. Chen, Y.C., Chiang, K., and Hartmann, S.R., 1980, *Phys. Rev. B*, **21**, 40.
4. Nakatsuka, H., Fujita, M., and Matsuoka, M., 1981, *Opt. Commun.*, **36**, 234.
5. Nakanishi, S. and Itoh, H., 1991, *J. Appl. Phys.*, **30**, L2042.
6. Koch, M., 1992, *Phys. Rev. Lett.*, **69**, 3631.
7. Beach, R., Hartmann, S.R., and Friedberg, R., 1982, *Phys. Rev. A*, **25**, 2658.
8. Friedberg, R. and Hartmann, S.R., 1993, *Phys. Rev. A*, **48**, 1446.
9. Friedberg, R. and Hartmann, S.R., 1994, *Bull. Rus. Acad. Sci.*, **58**, 1282.
10. Weber, K.-H. and Sansonetti, C.J., 1987, *Phys. Rev. A*, **35**, 4650.
11. Lu, X., Brownell, J.H., and Hartmann, S.R., 1995, *Opt. Commun.*, **120**, 295.
12. Kurnit, N.A., Abella, I.D., and Hartmann, S.R., 1964, *Phys. Rev. Lett.*, **13**, 567.